ELSEVIER SCIENCE B.V. [DTD 4.1.0]
JOURNAL APM ARTICLE No. 6246
PAGES 1-18 DISPATCH 2 April 2001
APM 6246
PROD. TYPE: FROM DISK
A

ELSEVIER

Applied Mathematical Modelling 000 (2001) 000–000

APPLIED MATHEMATICAL MODELLING

www.elsevier.nl/locate/apm

A sand surface element for efficient modeling of residual stress in castings

Daniel Metzger [a], K. Jarrett New [b], Jonathan Dantzig [a,*]

[a] *Department of Mechanical and Industrial Engineering, University of Illinois at Urbana-Champaign, 140 Mechanical Engineering Building, MC-224, 1206 West Green Street, Urbana, IL 61801, USA*
[b] *Ford Motor Company, USA*

Received 27 March 2000; received in revised form 4 December 2000; accepted 19 December 2000

Abstract

This article describes a method to efficiently predict residual stresses in foundry castings. We replace explicit modeling of the sand mold during stress analysis by using a locally applied boundary condition element. Methods are given for assigning appropriate values to the individual elements, and we present several example problems. In these test problems, we also evaluate several constitutive models for the sand. We find that plastic strains and displacements in the casting do not depend strongly on the sand constitutive model. Further, the stress states produced, when using the new surface elements, are generally in good agreement with those found using a full mold. The computational advantages of the new element are demonstrated. © 2001 Published by Elsevier Science Inc.

1. Introduction

1.1. Overview

Metal casting is a widely used manufacturing process for complex engineered parts. One of the most common casting methods is sand casting, where molten metal is poured into a mold composed of sand and a binder. The most common binder is a mixture of clay and water; this type of mold is called ''green sand''. The casting process is subject to defects, such as hot tears, cold cracking, and high residual stresses. Simulation is a potentially powerful tool for improving casting designs to mitigate these defects. However, for the simulations to be effective, they must be accurate and execute in a reasonable time.

One of the most popular methods for modeling the casting process is the finite element method (FEM). The major drawback in using the FEM is the large amount of time required to build the mesh, and to run the computations. For sand castings, much of the analysis time is consumed in computing temperatures, stresses and strains in sand mold, which in the end is of little use to the user.

* Corresponding author. Tel.: +1-217-333-4107; fax: +1-217-244-6534.
E-mail address: dantzig@uniuc.edu (J. Dantzig).

0307-904X/01/$ - see front matter
PII: S0307-904X(01)00017-8

This work describes the development of a surface element (SANDSURF) that replaces the sand mold in stress calculations by applying appropriate normal forces to the cast part. Fig. 1 illustrates the concept of the SANDSURF element, which is modeled as a nonlinear spring and ratchet combination. This approach is a continuation of the work by New [1], and Wiese and Dantzig [2].

The concept is similar to the boundary curvature method for heat flow, developed by Lu, Wiese and Dantzig [3–5], where the transient thermal problem is solved in the cast part using surface elements to represent the heat transfer characteristics of the sand mold. By combining the boundary curvature method for heat flow and the SANDSURF element, one can greatly reduce the analysis time for foundry casting simulations.

The surface element is implemented in ABAQUS™ using the user element function (UEL). The UEL is a subroutine that is called whenever information about the surface element is required. The UEL is designed as a four-noded quadrilateral element on the exposed surface of an eight-noded three-dimensional hexahedral element, where the mold would normally be in contact with the casting. The UEL supplies a normal force on the casting when the metal is displaced into the sand, i.e., in the positive normal direction, and when displaced in the negative normal direction, the UEL retains its previous position and no force is applied. This simulates crushing of the sand.

We investigated several models to compare the full mold and UEL material models. Since our goal is to predict residual stresses, we compare the plastic strains and nodal displacements in the metal using various constitutive relations and modeling approaches. In the following section, we introduce models for sand mechanical behavior, and then go on to a more detailed description of the surface element implementation. We then present several example problems which test the importance of the sand constitutive model, and the efficacy of using the new surface element.

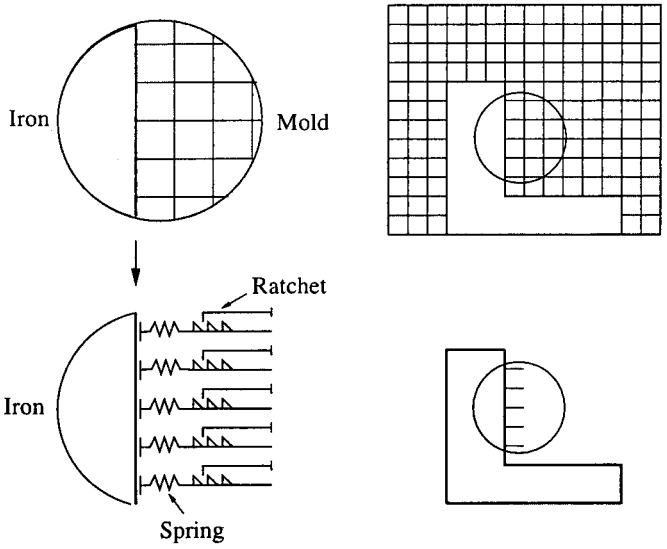

Fig. 1. Conceptualization of the sand surface element. The top right shows a metal part with a meshed mold. The circled area is the area expanded shown to the left. The bottom image shows the metal part with the sand surface element applied.

1.2. Soil mechanics

Although our goal is to eliminate the sand mesh from the analysis, to do this properly, an understanding of soil mechanics is required. Granular solids are composed of interlocking particles that form a skeleton. Within this skeleton are voids that hold liquid, gas, or a combination of the two. The void content is measured by the void ratio (e) which is the ratio of the total volume of the voids to the total volume of the solid particles, $e = V_v/V_s$. Terzaghi [6] developed the "effective stress" theory for granular materials, where the total stress is the sum of the stress in the skeleton (the effective stress $\boldsymbol{\sigma}'$) and the pore pressure u_w:

$$\boldsymbol{\sigma} = \boldsymbol{\sigma}' + u_w \boldsymbol{I}. \tag{1}$$

The pore pressure in the model is related to the degree of saturation, S_r with $0 < S < 1$, by the following expression (in units of kPa) [6]:

$$u_w = -\frac{3}{S_r} + \frac{0.006}{1 - S_r} - 1.4. \tag{2}$$

By definition, $u_w = 0$ for $S_r = 1$. When the material is partially saturated, the pore pressure becomes negative, producing a capillary vacuum within the voids.

Fig. 2 shows a typical relationship between the void ratio and hydrostatic pressure, $p = -\sigma_{ii}/3$. Virgin granular material has no past stress history. As the pressure is increased, the void ratio changes according to the virgin consolidation line (VCL) given by

$$e = \Gamma_{\mathrm{VCL}} - \lambda \ln p, \tag{3}$$

where Γ_{VCL} is the e axis intercept at $p = 1$, λ is the slope of the line, and p is the hydrostatic pressure. If the pressure is reduced or removed from the material, the void ratio follows the isotropic rebound line (IRL)

$$e = \Gamma_{\mathrm{IRL}} - \kappa \ln p. \tag{4}$$

The intersection of the VCL and IRL is defined as the pre-consolidation pressure, p_0. Continued loadings after the initial consolidation will follow along the IRL until the the pre-consolidation pressure is reached, after which the path follows the VCL.

A granular solid deforms differently depending on the hydrostatic pressure, sometimes called the confining pressure. When the confining pressure is low, under strain the material will initially try to consolidate, producing a volume decrease, until a peak stress is reached. At this point the

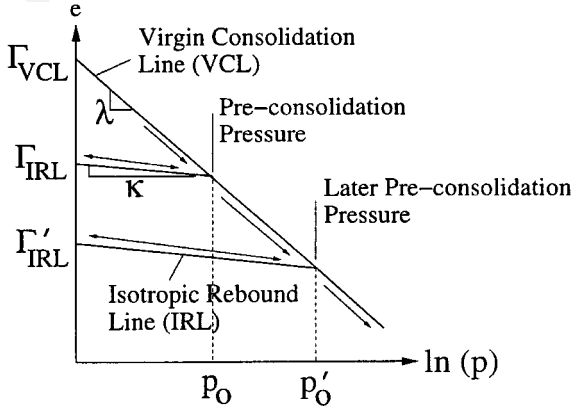

Fig. 2. Illustration of soil consolidation (after Terzaghi [6]).

particles start to slide over each other, producing a volume increase. This is termed *dilatant* behavior. When the confining pressure is higher, the material will consolidate into a denser configuration, referred to as *compactive* behavior. If strain continues to be applied, the void ratio reaches a "critical state", where further strain causes no change in the void ratio.

1.2.1. Modified Cam–Clay model

The modified Cam–Clay model (MCC) is commonly used to describe the behavior of soils, including foundry sands [7]. The MCC model features a yield surface that depends on hydrostatic pressure. It is easier to visualize the yield surface in p–q space, where p is the hydrostatic pressure, $p = -\sigma_{ii}/3$, and q is the magnitude of the deviatoric stress, $q = \sqrt{\frac{3}{2}S_{ij}S_{ij}}$, where $S_{ij} = \sigma_{ij} - p\delta_{ij}$.

We used the MCC model as it is implemented in ABAQUS™, and the reader is referred to the theory manual for ABAQUS™ for full details [8]. The MCC yield surface is an ellipse in p–q space, illustrated in Fig. 3, and given by the form

$$f(p,q) = q^2 + M^2 p(p-a) = 0, \tag{5}$$

where a is a parameter which defines the size of the yield surface from past deformation, and M is the (constant) slope of the critical state line (CSL). Any stress state within the present yield surface is considered to be elastic and reversible. Any stress state that reaches the yield surface changes the yield surface size, and is in the plastic regime. We note that ABAQUS™ permits a more general definition of the yield surface, including the possibility that the parameter M evolves during the simulation, but we simply choose M to be a constant.

The parameter a defining the size of the yield surface evolves with time according to

$$a = a_0 \exp\left[(1+e_0)\frac{1-\det \boldsymbol{J}^{\mathrm{pl}}}{\lambda - \kappa \det \boldsymbol{J}^{\mathrm{pl}}}\right], \tag{6}$$

where a_0 is the initial value of $a = p_0/2$, e_0 is the initial void ratio, and $\det \boldsymbol{J}^{\mathrm{pl}}$ represents the inelastic volume change. This is a statement in equation form of the plots in Fig. 2.

The CSL divides the p–q plane into two parts. On the left, or "dry side", the material demonstrates dilatant behavior, such that upon yielding the material softens and the yield surface shrinks. In this case, the void ratio increases as particles separate (see Fig. 4). If the stress state is on the right side, or "wet side", of the CSL the material will compact as it deforms. This is accompanied by strain hardening, and the yield surface expands (see Fig. 5). In both cases, the yield surface will continue to change until the stress state reaches the CSL, where the material can continue to deform with no change in p or q.

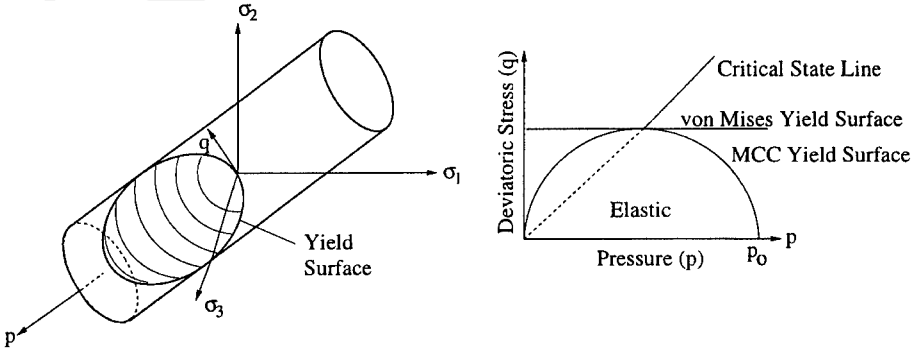

Fig. 3. MCC model yield surface in principal stress space and p–q stress space.

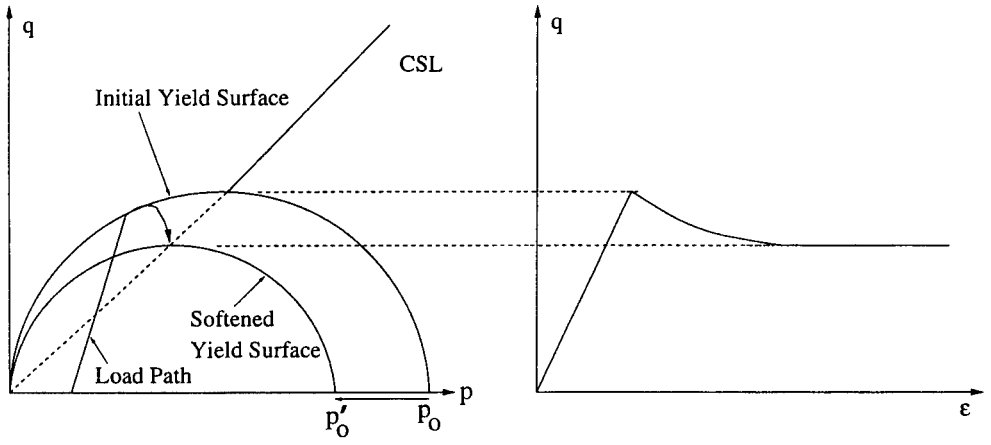

Fig. 4. Illustration of the modified Cam–Clay model dry side or dilatant behavior.

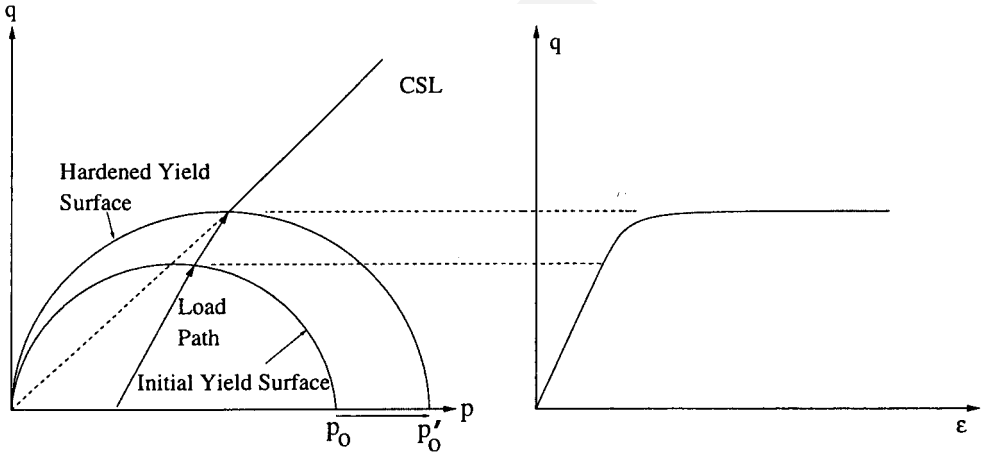

Fig. 5. Illustration of the modified Cam–Clay model wet side or compactive behavior.

Ami Saada et al. [7] investigated the thermomechanical behavior of casting sands. They conducted various deformation tests at temperatures up to 500°C. At temperatures above 120°C, they found that foundry sand exhibits dilatant behavior, and a compactive behavior at temperatures below 120°C. They also report a temperature-dependent elastic modulus ranging from 22 MPa at 25°C to 100 MPa at 500°C. A more comprehensive listing of the mechanical sand properties can be found in Appendix A.

2. Theory

2.1. Sand surface element

The sand surface element is based on assigning "appropriate" resistive forces to a casting surface, depending on the normal displacements of the surface nodes. The sand surface element is a linear four-noded quadrilateral element covering the four exposed nodes of a linear eight-noded

brick element. Since sand provides little shear resistance, only the normal components are considered.

To make the calculations simpler, we define a local coordinate system at each element and perform the calculations in this reference frame. ABAQUS™ requires that the stiffness and residual contributions from the user element be returned from the subroutine in the global coordinate frame. Before returning the stiffness and residual contributions to the main program, we convert them from the local to the global reference frame. This task is performed using the rotational and relational matrices, derived from the global coordinates.

The user element subroutine (UEL) is called every time information about a surface element is required. ABAQUS™ passes information to the routine including: the element's nodal coordinates, the present time step and time increment. The local displacements u'^{n+1} are then determined using the rotation matrix, and the global displacements, u^{n+1}. At the initial time step, the initial displacement is set as the maximum displacement. At subsequent time steps, u'^{n+1} is compared to the last stored maximum displacement, u'^{n}. If $u'^{n+1} \geqslant u'^{n}$ then there is contact between the mold and casting, the proper element stiffness is then assigned and u'^{n+1} is then stored as the new maximum displacement. Each element has a unique assigned stiffness, β, which we describe later. The updating of the maximum displacement allows the element to mimic plastic behavior in the sand. If $u'^{n+1} < u'^{n}$ then the casting is moving away from the mold, and a gap is formed [1]. In this case, if we were to assign a value of zero stiffness, the sudden discontinuity in resistance causes numerical difficulties. To solve this problem we employ a "soft contact" method based on the displacement away from the maximum sand location. We modify the applied stiffness to β' as

$$\beta' = \beta e^{-10(|u'^{n} - u'^{n+1}|)}, \tag{7}$$

where β is the stiffness if the casting is in full contact with the sand and $|u'^{n} - u'^{n+1}|$ is the displacement away from the current maximum displacement. The constant (10) was chosen, after substantial testing, because it was the largest value that provided easy convergence.

2.2. Assigning element stiffness

As a motivational prototype, consider the model sketched in Fig. 6. The mold stiffness on face **A** can be approximated as that of a column of sand running normal to the surface at **A** and

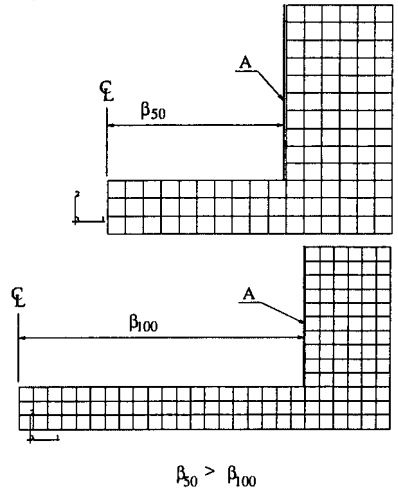

Fig. 6. Illustration of differences in UEL stiffness (β) for different compaction lengths (L).

terminated at the centerline where the displacement is zero. The stiffness of this column is $\beta = (E/L)$.

To determine the UEL elastic stiffness more systematically, consider the example of a one-dimensional sand "bar" analogous to that just described. We solve

$$\frac{d^2u}{dn^2} = 0, \tag{8}$$

where n is the coordinate normal to the casting into the sand. By setting boundary conditions of $u(0) = 1$ and $u(L) = 0$ and integrating, we find the strain in the sand bar to be

$$\frac{du}{dn} = -\frac{1}{L}. \tag{9}$$

Multiplying the strain by the modulus of elasticity (E) gives the normal stress, whose absolute value we identify as the bar's stiffness

$$\beta = E\frac{du}{dn}. \tag{10}$$

To generalize this approach to higher dimensions and curved surfaces, we construct an elastic sand mold without the casting present, and subject it to a unit normal displacement on each face, while keeping the outer boundary fixed. We then solve an elastic model for the sand. The normal strain at each element is then extracted, and we define β according to Eq. (10).

To describe the process in more operational detail, we generate a full mold mesh with surface elements placed at the metal–mold interface. A utility program is then run to calculate the unit normals and place boundary conditions on the metal–mold interface. The elastic mold problem is then analyzed in ABAQUS™. After this analysis, the stresses in the x, y, and z directions are extracted for each Gauss point on each surface element and then averaged. The average stress for each direction is then multiplied by its corresponding component of the unit normal

$$\begin{bmatrix} \sigma_{xx} & 0 & 0 \\ 0 & \sigma_{yy} & 0 \\ 0 & 0 & \sigma_{zz} \end{bmatrix} \cdot \begin{Bmatrix} \widehat{n_x} \\ \widehat{n_y} \\ \widehat{n_z} \end{Bmatrix} = \begin{Bmatrix} \beta_x \\ \beta_y \\ \beta_z \end{Bmatrix}, \tag{11}$$

where $\widehat{n_x}$, $\widehat{n_y}$, $\widehat{n_z}$ are the components of the normal vector, $\underline{\sigma_{xx}}$, σ_{yy}, σ_{zz} are the stresses, and β_x, β_y, β_z are the stiffness components. The magnitude ($\sqrt{\sum \beta_{ii}^2}$) of the β vector is used as the UEL stiffness.

We tried two methods for determining the stiffness. The simplest approach was to apply a unit normal displacement into the sand at all surfaces on the casting *at the same time*. This has the advantage of providing all of the stiffnesses in one analysis. However, we found more accurate results when we displaced the surface elements one at a time, performing a separate elastic analysis for each element stiffness. The results presented in the following section use this latter approach. We recognize that such an approach is inconvenient, and are currently examining more efficient hybrid schemes.

3. Results

3.1. Two-dimensional analysis

Here, we investigate the role of the sand constitutive model in determining the stress state during the solidification process. We used the MCC theory as a constitutive model for the sand, and sought the answers to the following questions:

- Does the sand deform elastically or does it yield?
- How does the level of saturation affect the result?
- How does the mold behavior affect the plastic strains and nodal displacements in the iron?
- Do we need a critical state soil model for the sand surface element?

To answer these questions, we constructed two-dimensional prototype models illustrated in Fig. 7 and observed the stress variations in the mold. We then looked at the plastic strains in the iron and how they depended on the sand constitutive model. Quantitative comparisons were made by comparing nodal displacements in the iron for each model, using the modified Cam–Clay model as the reference standard.

3.1.1. Analysis with full sand mold

The thermal analysis was performed using FIDAP™. Successive substitution with a maximum of thirty iterations was used to solve the nonlinear system of equations presented by the enthalpy formulation for the latent heat, and temperature-dependent properties. A listing of the thermal properties used is given in Appendix A. The transient problem was solved up to 6000 s using backward Euler integration with variable time steps.

After the thermal analysis was completed, the mesh and temperature history were converted into input files for ABAQUS™. In order to allow the mold and metal to separate during the mechanical analysis, duplicate nodes were added at the mold–metal interface, and gap elements were defined. The gap elements transfer normal loads but no shear. To simplify the presentation of the results, a single representative element (R) is chosen to represent the average sand behavior. Fig. 7 shows the location of the element (R) within the compaction area.

The two-dimensional model was analyzed as plane strain for two levels of saturation, $S_r = 0.1$ and $S_r = 1.0$. Fig. 8 shows (as circles) pressure vs. deviatoric stress, or p–q, plots for all elements in the model at 6000 s, for both degrees of saturation. The stress path for the representative element

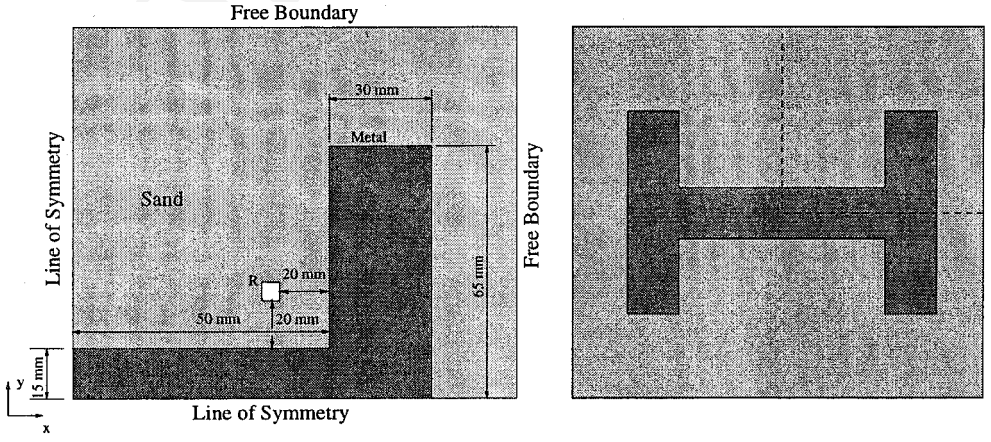

Fig. 7. Two-dimensional model schematic illustrating the representative element and boundary conditions.

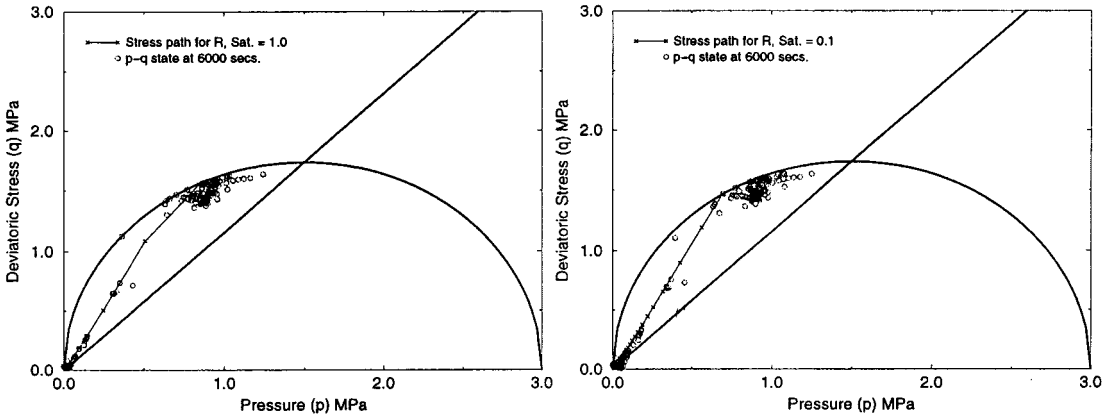

Fig. 8. MCC yield surface and CSL with stress data for the mold at 6000 s and the stress path for element (R) over time. The left-hand side figure shows saturation level of 1.0, and on the right the saturation level is 0.1.

(R) is also shown as a line. The stress does not reach critical state in any element, but there is plastic deformation in some elements, corresponding to those whose circles lie on the yield surface. This causes the observed bending of the points in the figure toward the CSL. It can be seen that there is little difference in stress history between the two saturation levels, and for both cases, the peak stress that the sand reaches before softening is 1.6 MPa.

3.1.2. Cast iron analysis

To illustrate the effect of the sand material models, we present the plastic strain in the iron after 6000 s for several cases. We conducted this analysis using the full sand mold analyses for the MCC model, an elastic–plastic, and linear elastic model.

An iterative process was used to obtain the elastic modulus for the elastic and elastic–plastic molds. The elastic modulus was varied by trial and error until the plastic strain magnitude contour plots of the iron appeared similar to those from the MCC analysis. This produced a value of 250 MPa for the elastic modulus which is somewhat higher than the value obtained by Ami Saada (100 MPa at 500°C). This difference can be attributed to using an entirely elastic, and two-dimensional analysis. The yield strength used in the elastic–plastic mold was taken to be the maximum deviatoric stress found in the MCC analysis, approximately 1.6 MPa.

Fig. 9 shows the plastic strain contours for all cases. The differences between the results for the two models which used the MCC model with different saturation levels are small. There are some differences between the MCC solutions and the elastic and elastic–plastic plots.

To better quantify the differences between the various cases, we conducted an error analysis using the nodal displacements of the iron in each model. We calculated the root mean square (RMS) error using the following:

$$\mathrm{RMS}\% = 100\sqrt{\frac{\sum(\Delta u)^2}{n}}, \tag{12}$$

where n is the total number of nodes and Δu is the difference in nodal displacement between the compared models. The maximum displacement percent error was calculated using

$$\text{Max. Disp.}\% = 100\left(\frac{\Delta u_{\max}}{u_1}\right), \tag{13}$$

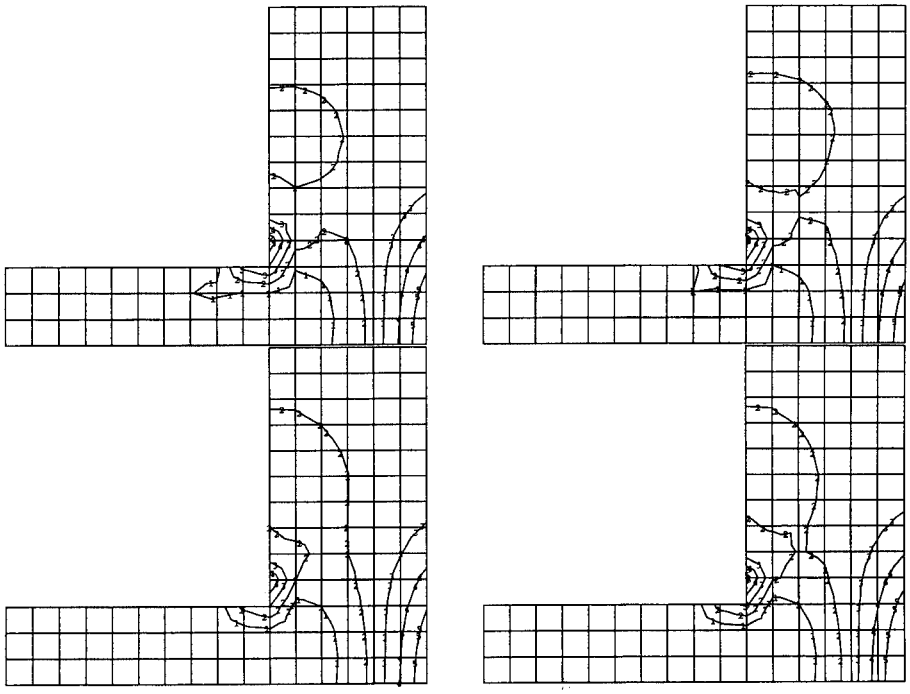

Fig. 9. Plastic strain magnitude in the iron model at 6000 s, two-dimensional analysis. Contour legend: (1) = 6.5E − 3, (2) = 6.57E − 3, (3) = 6.65E − 3, (4) = 6.7E − 3, (5) = 6.8E − 3. Clockwise from the upper left: MCC, saturation 0.1; MCC, saturation 1.0; U elastic–plastic; and elastic mold.

where the Δu_{max} is the maximum difference in nodal displacement and u_1 is the displacement for one of the models being compared.

Table 1 lists the results of this analysis. The differences between the two MCC models, and between the MCC and elastic–plastic models are small, typically less than 3% for the maximum displacement error. We tried variations of this geometry, and found similar results. This indicates that an elastic–plastic model could be used to model the sand behavior in these casting problems. The error associated with the MCC models and the linear elastic model, which is greater than the others, is still relatively small (<10%). This indicates that even a simple elastic model can capture most of the effect of the sand mold on the iron. We note that the elastic modulus we used here was

Table 1
Error analysis for the two-dimensional model

50 mm model	RMS (%)		Max. disp. (%)	
	x-direction	*y*-direction	*x*-direction	*y*-direction
MCC low[a] vs. MCC high[b]	0.38	0.08	2.31	0.43
MCC low vs. EP[c]	0.63	0.14	1.98	1.61
MCC low vs. E[d]	0.70	0.30	6.28	1.30
MCC high vs. EP	0.42	0.19	2.22	1.21
MCC high vs. E	1.03	0.37	8.39	1.64
EP vs. E	1.06	0.20	6.31	1.17

[a] Mold of MCC material, low saturation.
[b] Mold of MCC material, fully saturated.
[c] Mold of elastic–plastic material.
[d] Mold of elastic material.

artificially large. This issue is resolved in the full three-dimensional analysis described in the following section.

Table 2 lists the analysis times for the various cases. These runs were made on a SUN™ SPARC server 630 MP™ workstation operating at 133 MHz. These results show a significant difference in time between the MCC models and the elastic-based models. This analysis leads us to conclude that the sand mold can be modeled effectively with an elastic or elastic–plastic model instead of using the more complex MCC models. The elastic and elastic–plastic models provide similar strain patterns in the iron and are less costly to run.

3.2. Three-dimensional wedge model

The wedge model is a variant of the previous models where the dumbbell shape is rotated about the x-axis. Fig. 10 shows the model that was investigated. The full mold problem consisted of 4027 nodes. The UEL model was made up of 992 nodes. Both were made of eight-noded linear brick elements.

The temperature history was obtained using FIDAP™, as in the earlier problem. We interpolated the full mold solution onto a casting-only mesh to be used for the UEL analysis. The time increment was limited to a maximum of 50 s to allow for proper temperature interpolation when running ABAQUS™. The previous investigations showed that saturation had little affect on the results so we used only one variant of the MCC model, saturation equal to 0.1, for this analysis.

In addition to the MCC model, we ran full mold solutions with elastic and elastic–plastic models. We iterated the solution with different elastic moduli and yield strengths until we achieved agreement with the iron plastic strain contour plot from the MCC analysis. This procedure yielded an elastic modulus value of approximately 45 MPa and a yield strength value of approximately 0.5 MPa. We note that this is the approximate average of the values reported by Ami Saada [7] over the full temperature range. Fig. 11 shows the plastic strain magnitude in the iron at 6000 s. The differences between the MCC, the elastic and elastic–plastic models are acceptable.

Table 3 lists the root mean square and maximum displacement errors for these models. All the errors are below 10% indicating that the sand surface element appears to model the mold behavior well in these problems. Table 4 lists the stress analysis times for the two wedge models. The last entry represents the time it would take if the job were to be conducted using the boundary curvature method for the temperature, although this is not applicable to the full mold cases. As before, the time increment was limited to 50 s to allow for proper interpolation. It can be observed that the times associated with the sand surface elements are significantly shorter than the full mold solutions, by a factor of as much as 100 for this problem.

3.3. Simplified camshaft

Fig. 12 shows a simplified camshaft that was used to investigate a more complicated case involving bending. Axial contraction is restricted from the top and bottom of the shaft. This model

Table 2
Stress analysis times for two-dimensional models

Model	Time (s)
MCC low saturation	3196
MCC full saturation	971
Elastic–plastic	303
Elastic	287

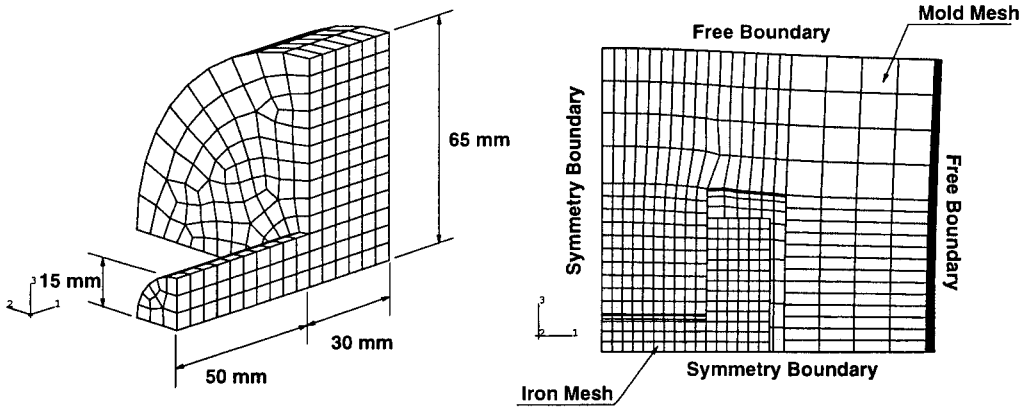

Fig. 10. Dimensions and boundary conditions on the 50 mm wedge model. Displaced mesh displacements magnified by 10. Left: solid mesh. Right: displaced mesh and boundary conditions.

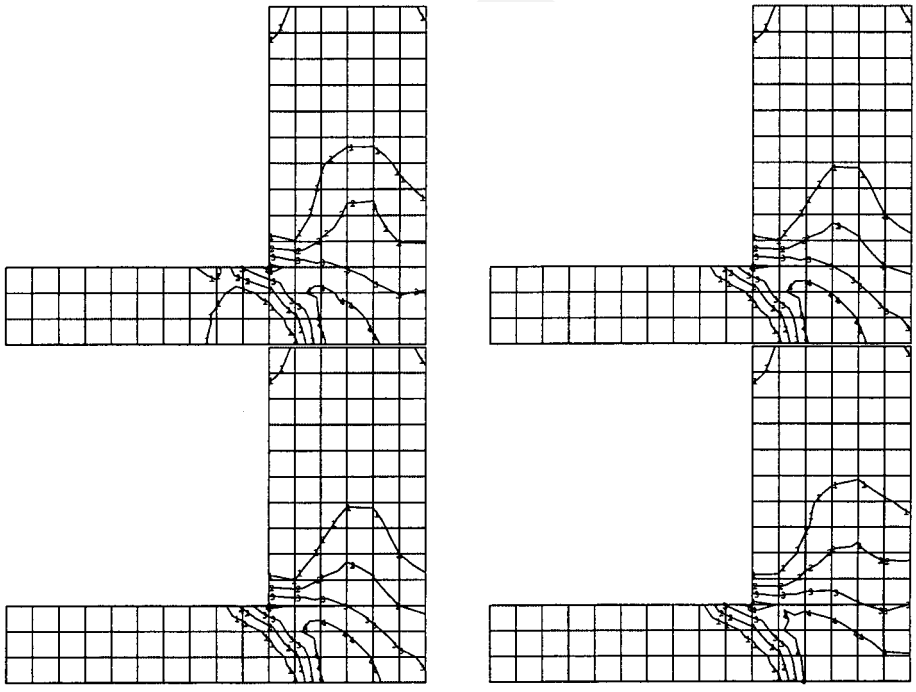

Fig. 11. Plastic strain magnitude at 6000 s, in the iron, for the 50 mm wedge model. Clockwise from the upper left: MCC, saturation 0.1; MCC, saturation 1.0; UEL; and Elastic mold plastic strain magnitude at 6000 s, in the iron, for the wedge model. Contour legend: (1) = 3.13E − 4, (2) = 6.27E − 4, (3) = 9.49E − 4, and (4) = 1.25E − 3. Clockwise from the upper left: MCC, saturation 0.1; MCC, saturation 1.0; UEL; and elastic mold.

is composed of a circular shaft with an eccentric cam at one end. This model has 5619 nodes in the full mold and 733 nodes in the UEL model, both constructed with eight-noded linear brick elements. The temperature solution is obtained in the same manner as the previous problems.

For this case, the displacement results from the full mold and user element solutions differ more significantly. Fig. 13 shows the displaced mesh for both cases at 3000 s. The sand surface element

Table 3
Error analysis for wedge models

50 mm Model at 6000 s	RMS disp. error (%)			Max disp. error (%)		
	x-direction	*y*-direction	*z*-direction	*x*-direction	*y*-direction	*z*-direction
MCC[a] vs. EP[b]	2.942	0.150	0.147	6.967	2.495	2.495
MCC vs. E[c]	2.868	0.145	0.143	6.742	2.479	2.477
MCC vs. UEL[d]	2.723	0.215	0.010	6.025	2.154	2.178
EP vs. E	0.075	0.0068	0.0066	0.211	0.098	0.098
EP vs. UEL	0.324	0.286	0.130	1.162	1.983	1.072
E vs. UEL	0.269	0.284	0.128	0.953	1.966	1.066

[a] Mold of MCC material, low saturation.
[b] Mold of elastic–plastic material.
[c] Mold of elastic material.
[d] Mold simulated with UEL.

Table 4
Stress analysis times for the wedge models

Model	Execution time (s)
MCC low saturation	103,922
Elastic–plastic	5676
Elastic	5634
Sand surface element	2777
Boundary curvature method	1043

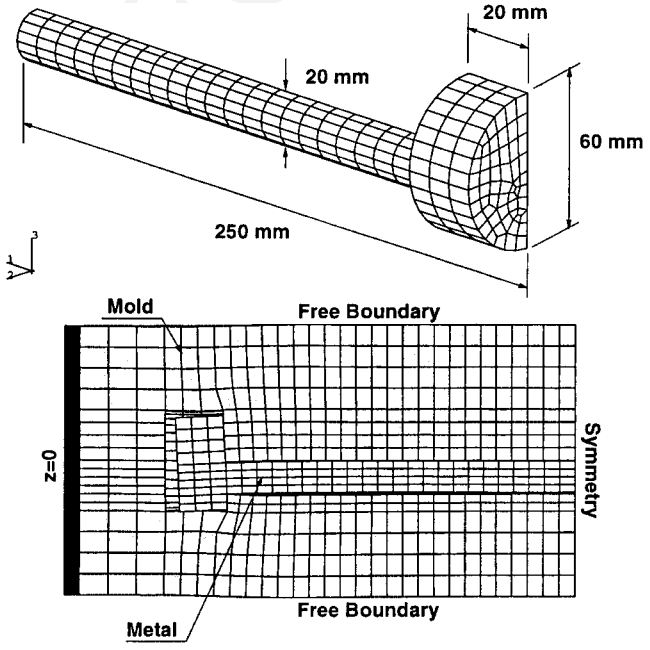

Fig. 12. Dimensions and boundary conditions on the 250 mm simplified camshaft model. Displaced mesh is magnified by 3.

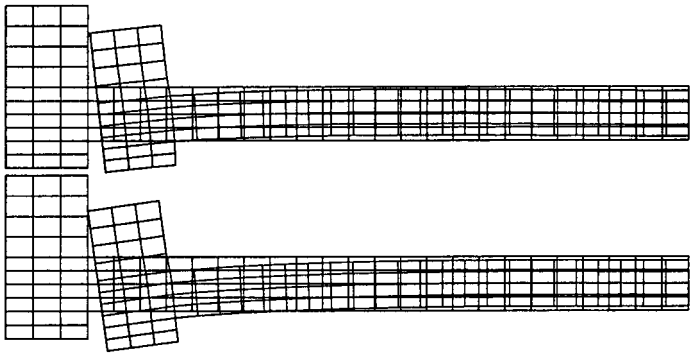

Fig. 13. Displaced meshes of the simplified camshaft for the full mold and UEL molds at 3000 s. Displacements magnified by 10.

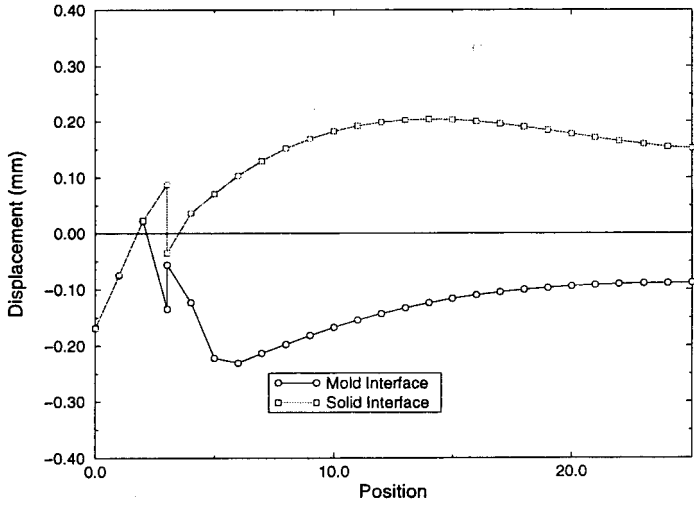

Fig. 14. Displacements in the z-direction, at 3000 s, along the bottom edge of the simplified camshaft for the metal and the elastic mold.

model's maximum displacement is larger than the full mold model and the user element model does not bow up as much as the full mold.

It can be seen from Fig. 12 that some unexpected displacements occur at the bottom mold–metal interface. Fig. 14 shows the displacements along the bottom edge of the casting, and it can be seen that the mold and metal are in contact only at the cam head. The mold has also been displaced in the positive z-direction above the reference line. This illustrates a continuum effect resulting from the fact that the full mold elements are coupled together, whereas each sand surface element is an individual entity.

This shows that the full mold cases have some continuum effects, depending on the geometry, that the sand surface element presently does not capture. Future work might include coupling the sand surface elements so that each element is aware of the movements of its neighbors.

Table 5
Thermal properties of silica sand with 7% bentonite and 4% water [9]

Temperature (°C)	k (W/mm K)	Temperature (°C)	c_p (J/g K)
25.0	0.733E − 03	27.0	0.676
200.0	0.640E − 03	127.0	0.858
400.0	0.586E − 03	327.0	0.993
600.0	0.590E − 03	527.0	1.074
800.0	0.640E − 03	727.0	1.123
1000.0	0.703E − 03	927.0	1.166
1400.0	0.829E − 03	1127.0	1.201
		1327.0	1.203
		1400.0	1.203

Table 6
Sand mechanical properties for use with the modified Cam–Clay model[a]

Variable		Value	Reference
λ	VCL slope	0.0896	[7]
κ	IRL slope	0.001	[7]
v	Poisson's ratio	0.24	[1]
M	CSL slope	1.157	[7]
p_o	Initial yield surface	3.0 MPa	[7]
k	Permeability	0.03 mm/s	[11]
e_0	Initial void ratio	0.64	[7]
σ'	Initial effective stress	0.05 MPa	Assumed
sat	Degree of saturation	0.1–1.0	Assumed
u_w	Pore pressure	0.0–(−0.03) MPa	[12]

[a] Properties taken at 300°C.

Table 7
Cast iron thermal properties

Temperature (°C)	k (W/mm K)	Temperature (°C)	c_p (J/g K)
0.0	6.686E − 02	0.0	0.0
100.0	5.950E − 02	99.85	53.934
200.0	5.560E − 02	199.85	109.282
300.0	5.030E − 02	299.85	165.964
400.0	4.520E − 02	399.85	223.981
500.0	4.000E − 02	499.85	283.413
600.0	3.510E − 02	599.85	344.098
700.0	3.301E − 02	699.85	406.975
800.0	2.972E − 02	799.85	474.325
900.0	2.600E − 02	899.85	541.675
1000.0	2.227E − 02	999.85	612.730
1145.0	2.227E − 02	1099.85	685.230
1200.0	2.227E − 02	1126.7	705.067
1500.0	2.227E − 02	1129.4	707.142
		1132.2	709.363
		1135.0	711.597
		1136.0	712.395
		1136.5	720.365
		1144.5	968.966
		1145.0	976.040
		1199.9	1024.612
		1299.9	1116.014
		1500.0	1298.551

4. Conclusions

Predicting residual stresses in foundry castings using the FEM is currently very costly. The process requires that the mold be discretized along with the cast part and included in the mechanical analysis. This limits the feasibility of performing an analysis on large castings because of the amount of time required to run the simulations. In addition, mold information data, such as stress and strain, are of little use to the end user.

We have developed a four-noded surface element (SANDSURF) that replaces the sand mold by applying appropriate normal forces to the casting surface, depending on the normal nodal displacements. This element was developed for use with ABAQUS™, but could be easily modified for use with other finite element codes.

Several two- and three-dimensional problems were presented to investigate the importance of soil mechanics models in casting analysis, and to compare the differences between the full mold and the UEL solutions. Models using the modified Cam–Clay, elastic and elastic–plastic molds were used. We determined that the modified Cam–Clay model is a costly model to use, and adds little accuracy when predicting residual stresses. We conclude that an elastic or elastic–plastic constitutive model would be sufficient. We found good agreement between the full mold and UEL solutions.

We uncovered some limitations of the UEL approach when comparing to full mold simulations. Discrepancies appear when complicated mold deformations are present. This is caused by the full mold's elements being coupled while the UEL's elements are isolated from each other. Possible future work may include coupling the nodal displacements of each element to its neighboring elements and defining some displacement rules to try to capture some of the different mold behaviors.

Appendix A. Material properties

The material properties used in the simulations are given in this section. Thermal and mechanical sand mold and iron properties are presented separately. Estimations had to be made for the iron at high temperatures, above 600°C.

A.1. Sand properties

Table 5 lists the thermal conductivity (k) and specific heat (c_p) used in the full mold simulations and also in the boundary curvature method calculations [3–5]. These data are based on silica sand composed of 7% bentonite and 4% water. The density was assumed to have a constant value of $1.52E-3$ g/mm^3 [9]. The initial temperature of the sand was 25°C.

Table 6 lists the data used in the modified Cam–Clay model. The VCL slope, λ, is obtained from [7, Fig. 12] and the following equation [10]:

$$\lambda = \frac{\Delta e_\lambda}{2.303 \log(p_1/p_0)}. \tag{A.1}$$

The slope of the IRL is found in a similar way

$$\kappa = \frac{\Delta e_\kappa}{2.303 \log(p_1/p_0)}. \tag{A.2}$$

Table 8
Cast iron mechanical properties [1,13]

Temperature (°C)	v	E (MPa)	Temperature (°C)	α (1/°C)
20.0	0.21	11.7E + 04	25.0	1.525E − 05
300.0	0.21	11.0E + 04	374.25	1.639E − 05
400.0	0.21	10.6E + 04	608.40	1.7956E − 05
500.0	0.21	10.5E + 04	727.5	1.993E − 05
600.0	0.21	7.6E + 04	797.58	2.2668E − 05
800.0	0.21	3.4E + 04	933.75	2.5765E − 05
1136.0	0.21	9.25E + 02	1136.0	2.9220E − 05
			1136.5	1.000E − 10
			1145.0	1.000E − 10

Table 9
Cast iron composition used for the stress–strain information [13]

	C	Si	Mn	S	P	Ni	Cr	Mo
Content (%)	3.16	1.50	0.67	0.111	0.24	0.59	0.37	0.59

Ami Saada et al. [7] show the CSL slope to be 1.157. The sand permeability range is 10^{-2}–10^{-4} mm/s [11]. The initial yield surface, p_0, was taken from at 300°C. The pore pressure, u_w, is taken for a corresponding degree of saturation.

A.2. Iron properties

Table 7 lists the thermal conductivity (k) and specific heat (c_p) used for the iron. The density of the iron was assumed constant at 7.0E − 3 g/mm^3.

Table 8 lists the mechanical properties for the cast iron used in the analysis. We were able to obtain elastic modulus data for temperatures only up to 600°C from the *ASM Specialty Handbook* [13]. We chose to use the Cr–Ni–Cu iron curve from the ASM Specialty Handbook [13].

For temperatures above 600°C, some estimations were made. When the iron enters the two phase region, between 1136° and 1145°C, the elastic modulus will decrease until it reaches the liquid phase, where it is zero. This causes numerical difficulties, so the liquid is given an arbitrary low elastic modulus so that the problem can be run. To eliminate a sudden drop in the modulus that might cause numerical problems, the transition between the solid and liquid phases was taken to be linear from 800°C to 1136°C.

Stress–strain curves were entered as bilinear forms at seven different temperatures, as shown in Fig. 15. Each curve is parameterized by two points, one for the yield point and the other for the ultimate stress. We were able to gather stress–strain information for temperatures only up to 600°C. This information is for a low alloyed gray iron. Table 9 lists the composition for the iron used. The composition of this material is not the same as that used for the elastic modulus data, the error is assumed to be small. Since all of the analyses in this paper are comparative, the effect of the estimates for material properties is expected to be small.

For temperatures above 600°C, we estimated the curves by assuming a yield stress and ultimate strength. This may lead to some errors but it is believed that they will be small at elevated temperatures. These curves are based on tension information only, the strength increase due to compression was not included.

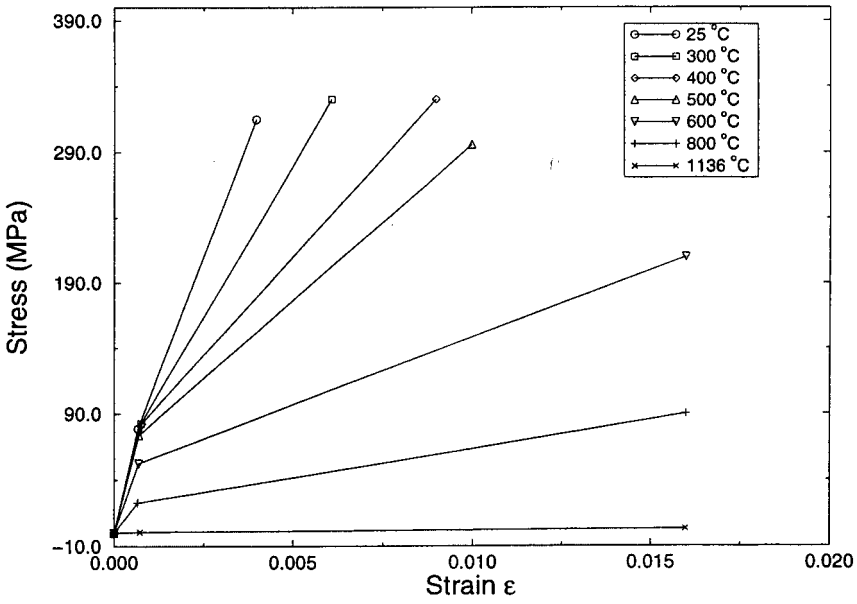

Fig. 15. Cast iron stress–strain curves for varied temperatures [13,14]. Tension curves only.

References

[1] K.J. New, An improved method for simulating the contact resistance of sand molds on gray iron castings, Master's thesis, University of Illinois at Urbana-Champaign, 1997.
[2] J.W. Wiese, J.A. Dantzig, Modeling stress development during the solidification of gray iron castings, Metall. Trans. A 21 (1990) 489–497.
[3] J.A. Dantzig, S.C. Lu, Modeling of heat flow in sand castings: Part I. The boundary curvature method, Metall. Trans. B 16 (2) (1985) 195–202.
[4] J.A. Dantzig, J.W. Wiese, Modeling of heat flow in sand castings: Part II. Applications of the boundary curvature method, Metall. Trans. B 16 (2) (1985) 203–209.
[5] J.W. Wiese, J.A. Dantzig, SPIDER and the boundary curvature method: simulating the solidification of foundry castings, Appl. Math. Model. 12 (1988) 213–220.
[6] K. Terzaghi, R. Peck, in: Soil Mechanics in Engineering Practice, second ed., Wiley, New York, 1967.
[7] R. Ami Saada, G. Bonnet, D. Bouvard, Thermomechanical behavior of casting sands: experiments and elastoplastic modeling, Int. J. Plasticity 12 (3) (1996) 273–294.
[8] Hibbitt, Karlsson, and Sorensen, Inc., Pawtucket, RI, ABAQUS/Standard Theory Manual, version 5.7., 1997.
[9] R.D. Pehkle, A. Jeyarajan, H. Wada, Summary of thermal properties for casting alloys and mold materials, Technical Report, Department of Materials and Metallurgical Engineering, University of Michigan, December 1982.
[10] R. Whitlow, in: Basic Soil Mechanics, second ed., Longman, New York, 1990.
[11] A. Schofield, P. Wroth, in: Critical State Soil Mechanics, McGraw-Hill, London, 1968.
[12] D. Bovet, P. Jouanna, E. Recordon, C. Saix, Experimental studies, Modern Issues in Non-Saturated Soils (357) (1995) 159–190.
[13] J.R. Davis (Ed.), ASM Specialty Handbook, American Society of Metals, Cleveland, OH, 1996.
[14] R. McDavid, Cast iron stress-strain information, private communication, Caterpillar Inc., October 1998.